Chemical Engineering Journal 484 (2024) 149454

Contents lists available at ScienceDirect

Chemical Engineering Journal

journal homepage: www.elsevier.com/locate/cej

In situ growth of copper nanoparticles in nitrogen-doped carbonized wood for efficiently enhancing its capacitive performance and electrocatalytic hydrogen evolution

Hewei Hou [a,b], Huashuang Huo [a,b], Yuanyuan Yu [a,b], Moyan Li [a,b], Yangyang Chen [a,b], Changzhou Chen [a,b], Guangfu Qian [a,b,*], Douyong Min [a,b,*]

[a] College of Light Industry and Food Engineering, Guangxi University, Nanning 530004, China
[b] Guangxi Key Lab of Clean Pulp & Papermaking and Pollution Control, Nanning 530004, China

ARTICLE INFO

Keywords:
Carbonized wood
Nitrogen-doped
Copper nanoparticles
Supercapacitor
Hydrogen evolution reaction

ABSTRACT

The development of self-supporting electrodes using natural wood is promising for energy storage and conversion but still challenging. Here, the nitrogen-doped carbonized wood electrode decorated with copper nanoparticles is synthesized to escalate its capacitive performance and HER. $Cu_{1.0}$NPs@NCW-1000 exhibits a high specific capacitance of 10.39 F cm^{-2} at 1 mA cm^{-2}. The symmetric supercapacitor achieves an energy density of 0.59 mWh cm^{-2} at 3.5 mW cm^{-2} while achieving a capacitance retention of 89.51 % after 8,000 cycles. $Cu_{1.0}$NPs@NCW-1000 also displays good HER activity, comprising an overpotential of 100.43 mV at 10 mA cm^{-2} and a Tafel slope of 95 mV dec^{-1}. Its outstanding properties were attributed to doping-nitrogen, high specific surface area, hierarchical porous structure, and the interaction between Cu NPs and NCW, which increased active sites and accelerated charge transfer. This work provides a new strategy for the preparation of self-supported carbon electrodes for the energy storage and electrocatalysis applications.

1. Introduction

The fossil energy shortage and increasing environmental pollution have become hot issues closely related to the development of human society in recent years [1], and the development of sustainable clean energy to replace fossil resources has become more urgent. Hydrogen, characterized by a wide range of sources, non-pollution, and high calorific value, is considered to be the most desirable alternative to fossil resources in the future [2,3]. Hydrogen produced from water electrolysis at the cathodic (hydrogen evolution reaction, HER) has received widespread attention as a promising hydrogen production technology with the advantages of simplicity, speed, and cleanliness. At present, although Pt/Ir/Ru exhibit excellent catalytic performance in the HER process, the problems of high cost and low storage capacity limit their industrial application [4,5].

Meanwhile, the development of advanced energy conversion and storage installations for the efficient utilization of energy is also crucial. Supercapacitors are highly regarded for their advantages of environmental friendliness, high power, and high cycle lifetimes, among the numerous energy storage devices [6–10]. However, the low energy density of supercapacitors has severely hindered their wide application. Whether it is supercapacitor or HER, the research focuses on the synthesizing of economical and environmentally friendly electrode materials with good performance [11].

Carbonized wood has become a promising carbon precursor to directly prepare self-supported electrodes for energy storage and electrocatalytic applications as a result of its high specific surface area, stable physicochemical properties, good electrical conductivity, abundant active sites, and tunable porosity [12,13], but the supercapacitor and HER performance of carbonized wood need to be improved. As reported in the literature, nitrogen-doped modification of carbon materials can increase the defect sites of the materials, enhance the electrical conductivity and the hydrophilic properties of the materials, thus improving the capacitive properties and enhancing the electrocatalytic HER activity [14–16]. For example, Liu et al. were able to obtain a nitrogen-doped carbon electrode from natural biomass which exhibited more excellent specific capacitance [17]. Hu et al. synthesized MoS_2 on porous carbonized wood as self-supported electrodes, which

* Corresponding authors at: College of Light Industry and Food Engineering, Guangxi University, Nanning 530004, China.
E-mail addresses: qianguangfu@gxu.edu.cn (G. Qian), mindouyong@gxu.edu.cn (D. Min).

https://doi.org/10.1016/j.cej.2024.149454
Received 26 November 2023; Received in revised form 27 January 2024; Accepted 6 February 2024
Available online 14 February 2024

significantly improved the HER performance [18].

Copper is an excellent pseudo-capacitive material with highly electrically conductive, abundant reserves, easy recycling, low price, etc. Besides, copper also has certain HER performance. Recently, Pandian et al. anchored copper nanoparticles in B-doped graphene nanoflakes as a negative electrode which enhanced the specific capacitance of the supercapacitor [19]. Aparna et al. prepared a composite with an efficient HER activity by loading copper nanoparticles onto amine-functionalized zirconium-based MOF scaffolds [20]. Furthermore, copper nanoparticles (Cu NPs) grown on carbon materials can enhance the conductivity of the electrodes and further improve the specific capacitance of electrodes. Meanwhile, loading Cu NPs into carbon materials to obtain carbon-based catalysts can provide efficient active sites and further enhance the HER catalytic activity of materials [21]. However, the combination of carbonized wood, nitrogen-doped, and Cu NPs has rarely been used for supercapacitors and HER, and the reasons for the improved performance also need to be further explored.

Herein, nitrogen-doped carbonized wood electrodes with *in situ* grown copper nanoparticles (denoted as Cu_xNPs@NCW-y, x represents the impregnation concentration of Cu^{2+}; y refers to the annealing temperature) by using natural wood as a carrier were prepared. $Cu_{1.0}$NPs@NCW-1000 was endowed with characteristics of high specific surface area, plentiful active sites, excellent hierarchical porous structure, and fast charge transfer rate by nitrogen-doped and growth of Cu NPs, which enhanced its capacitance and HER catalytic performance. As a result, the $Cu_{1.0}$NPs@NCW-1000 electrode showed a high specific capacitance of 10.39 F cm^{-2} (305.57 F g^{-1}) at 1 mA cm^{-2}. The assembled symmetric supercapacitor (SSC) not only outputted a high energy density of 0.59 mWh cm^{-2} at a power density of 3.5 mW cm^{-2}, but also had a capacitance retention rate of 89.51 % after 8,000 cycles. Meanwhile, the $Cu_{1.0}$NPs@NCW-1000 catalyst displayed a favorable HER activity with a low overpotential of 100.43 mV at 10 mA cm^{-2}, and the working potential did not show any significant change and the polarization curve only shifts by 12 mV after a continual operation at 100 mA cm^{-2} for 65 h. Thus, this work combined the advantages of non-precious metal nanoparticles with self-supported nitrogen-doped carbonized wood electrodes for supercapacitors and HER, provided an important reference for synthesizing the multifunctional electrode materials.

2. Experimental

2.1. Materials

Pine wood was obtained from Linyi Beimu Wood Products Co., Ltd. (Linyi, China). Concentrated hydrochloric acid (HCl, 36 wt%), ammonium chloride (NH_4Cl, 99.5 wt%), anhydrous ethanol (Ethanol 98 wt%), Copper chloride dihydrate ($CuCl_2$ $2H_2O$, 99 %) and potassium hydroxide (KOH, 85 wt%) were purchased from Nanning Rongyi Experimental Equipment Co., Ltd. (Nanning, China). All reagents were used without further purification.

2.2. Preparation of NCW

Pine wood was cut into 20 × 20 × 2.5 mm^3 along the growth direction and then soaked in 80 °C deionized water for 8 h to remove most of the inorganic salts and extractives, resulting in the dredging effect of the fiber cell channels. Following air-drying, the wood pieces were pre-oxidized at 220 °C (1 °C /min, annealing for 4 h) in a blast-drying oven. The pre-oxidized wood pieces were impregnated with 28 % NH_4Cl solution in vacuum for 24 h followed by a vacuum drying at 60 °C. The dried wood was carbonized at 1000 °C in a tube furnace under argon atmosphere (5 °C/min, argon flow rate of 10 sccm, and annealing for 3 h) to acquire the nitrogen-doped carbonized wood (NCW). The self-activated carbonized wood (SCW) was subjected to the same conditions except that it was not vacuum impregnated with NH_4Cl solution.

2.3. Preparation of Cu_xNPs@NCW-y

The NCW was impregnated with 1.0 M $CuCl_2$ solution in vacuum for 12 h, dried in a vacuum oven at 60 °C, and then carbonized at 1000 °C in a tube furnace under argon atmosphere (5 °C/min, flow rate of 50 sccm, and annealing for 3 h) to enable Cu NPs load on NCW ($Cu_{1.0}$NPs@NCW-1000). As the comparison samples, the electrodes with different Cu^{2+} concentration loadings were prepared by changing only the impregnation concentrations to 0.5, 0.8, and 1.2 M under the same condition, the electrodes with different annealing temperatures were prepared by changing only the temperatures at 600 °C and 800 °C under the same condition. The samples were represented by Cu_xNPs@NCW-y (x represents the impregnated Cu^{2+} concentration, y represents the annealing temperature).

2.4. Material characterization

The morphology, microstructural, and element distribution of the samples were obtained by scanning electron microscopy (SEM, ZEISS sigma300, Germany) equipped with energy dispersive spectroscopy (EDS, Oxford Ultim Max40). The Brunauer-Emmett-Teller (BET) specific surface area, the elemental content, X-ray diffraction patterns, Raman spectra, and the surface chemical information of the samples were obtained by a specific surface area and pore volume analyzer (MICROMERITICS, ASAP 2460, U.S.A.), an inductively coupled plasma optical emission spectrometry analyzer (ICP-OES, Agilent 720ES), an X-ray diffractometer (XRD, MINFLEX600, Japan) with Cu Kα radiation, a laser Raman spectrometer (Raman, in Via Reflex, England) with a laser wavelength of 532 nm, and an X-ray photoelectron spectroscopy (XPS, Thermo Scientific K-Alpha).

2.5. Electrochemical measurement of the supercapacitor

A multi-channel electrochemical workstation (INTERFACE 1000, USA) was used to perform cyclic voltammetry (CV), galvanostatic charge–discharge (GCD), and electrochemical impedance spectroscopy (EIS) with a typical three-electrode system in 2.0 M KOH electrolyte at 25 °C. During the tests, Ag/AgCl, Pt (2 × 2 cm^2), and Cu_xNPs@NCW-y electrode (1 × 1 × 0.1 cm^3) were employed as reference, counter, and working electrodes, respectively. Cycle life measurements were run on LANDCT2001A (China). The area specific capacitance (C_s, F cm^{-2}), mass specific capacitance (C_m, F g^{-1}), and volume specific capacitance (C_v, F cm^{-3}) were calculated as follows:

$$C_s = (I \times \Delta t)/(S \times \Delta V) \quad (1)$$

$$C_m = (I \times \Delta t)/(m \times \Delta V) \quad (2)$$

$$C_v = C_s/d \quad (3)$$

Where I (A), ΔV (V), Δt (s), S (cm^2), m (g), d (cm) represent the discharge current, voltage drop, discharging time, electrode area, electrode mass, and electrode thickness.

The energy density (E, Wh kg^{-1}) and power density (P, W kg^{-1}) the symmetric supercapacitors were calculated by the following equations:

$$E = \left(C \times \Delta V^2\right)/2 \times 3.6 \quad (4)$$

$$P = 3600E/\Delta t \quad (5)$$

2.6. Electrochemical measurement of HER

Electrochemical impedance spectroscopy (EIS), Linear voltametric scanning (LSV), and chronopotentiometry (CP) were tested in N_2-saturated 1.0 M KOH electrolyte at 30 °C with a typical three-electrode system. Hg/HgO, graphite rods, and $Cu_{1.0}$NPs@NCW-1000 were used as the reference electrode, counter electrode, and working electrode.

Frequency range of EIS was from 0.1 to 100,000 Hz, and the amplitude was of 5 mV. All the measured potentials *vs.* RHE were converted by the following equation [22]:

$$E_{HER} = E_{Hg/HgO} + 0.098V + 0.059pH - IR \quad (6)$$

Where $E_{Hg/HgO}$ and R are measured potential and solution resistance.

The cyclic voltammetry (CV) was performed in the non-Faraday zone to calculate the C_{dl} of the catalyst and derive the electrochemical active area (*ECSA*) using the following equation [23]:

$$ECSA = C_{dl}/C_s \quad (7)$$

Where C_s is the specific capacitance, and C_{dl} is obtained by testing CV at different scan rates in a non-Faraday zone.

The Tafel slopes were calculated by a linear fit using the following formula [24]:

$$\eta = b \times \log j + a \quad (8)$$

Where η, b, and j are the Tafel slope, overpotential and current density.

3. Results and discussion

3.1. Materials characterizations

The fabrication of self-supported carbonized wood electrodes *in situ* grown Cu NPs was shown in Fig. 1 (Cu_xNPs@NCW-y). In this process, the pre-oxidized wood (Fig. S1b) was obtained by annealing the natural wood (Fig. S1a) in an air atmosphere at 220 °C, which introduced oxygen-containing functional groups, enhanced the cross-linking of lignin and cellulose, and formed a stable chemical structure to avoid deformation during the carbonization process [25]. Afterward, the pre-oxidized wood was impregnated with ammonium chloride solution and annealed at a low gas flow rate of 1000 °C, yielding nitrogen-doped carbonized wood which showed a milder dimensional shrinkage during annealing compared to SCW, probably because nitrogen-doped stabilized its structure to some extent (Fig. S1b, c). The micro-morphology of NCW exhibited uniformly distributed anisotropic micrometer-sized channels (20–30 μm, Fig. 2a) and open vertical channels (Fig. 2d), which served as an important channel for electrolyte transport, storage, and can facilitate rapid electrolyte transport and the escape of gases during supercapacitor and HER process [26]. Besides, a large number of nanopores (Fig. 2a-f) etched out during the nitrogen-doped process were present on the surface and cross section of NCW, which further improved the specific surface area, promoted rapid electrolyte transport, and provided more effective buffer space for energy storage.

Finally, NCW was vacuum impregnated in different concentrations of $CuCl_2$ solution, and then Cu NPs were grown *in situ* in the open channels of NCW by modifying annealing temperatures to obtain Cu_xNPs@NCW-y (Fig. S1e). As demonstrated in Fig. 2g-i, numerous particles (AD = 58.6 nm) were uniformly immobilized in the open tubular cells of $Cu_{1.0}$NPs@NCW-1000, which were identified by the subsequent XRD mapping as Cu NPs. The uniformly grown Cu NPs can be considered as pseudocapacitive substances and HER active sites for enhancing the capacitive and catalytic properties of materials [19,27]. Subsequently, we obtained the microscopic morphology of Cu_xNPs@NCW-y impregnated with different Cu^{2+} concentrations by SEM images (Fig. 2i and Fig. S2). Obviously, the size of Cu NPs decreased and then increased as the impregnation concentration of Cu^{2+} was increased from 0.5 M to 1.2 M, which was due to the high degree of graphitization of NCW obtained at the annealing temperature of 1000 °C. When the impregnation concentration was low, it was difficult for the solution to uniformly fill the interior of the NCW by the interfacial effect and surface tension, and it accumulated on the surface and edge of the electrode. After the impregnation concentration was further increased, the interfacial effect was broken, and the solution began to fill the entire interior of the wood pipeline uniformly and combined with the abundant nucleation sites inside to grow into uniform Cu NPs, which began to aggregate to form larger-sized Cu NPs as the concentration of Cu^{2+} impregnation was further increased. Among them, the distribution of Cu NPs obtained at an impregnation concentration of 1.0 M was more homogeneous, which could expose more active sites to further improve accessibility of the electrolyte. Then, the uniform distribution of C, N, O and Cu elements throughout the structure was confirmed by the elemental mapping (Fig. 2 j), demonstrating that the nitrogen element was successfully doped, and the uniformly grown particles were Cu NPs.

The pore structure was further characterized by N_2 adsorption–desorption experiments, and type IV isotherms confirmed the existence of numerous micropores and mesopores (Fig. 3a, b) in all the samples, which were used to maintain transportation channels for the permeation of electrolyte ions to facilitate the dynamic exchange process of the electrolyte ions and the escape of gases during the HER process [28,29]. Moreover, the microporous volume of NCW was significantly increased compared to SCW due to the increased specific surface area by nitrogen doped. And the specific surface area of NCW reached 1220.92 $m^2\ g^{-1}$ with an average pore size of only 2.01 nm and a microporosity of 46.94 % (Table S1). Notably, $Cu_{1.0}$NPs@NCW-1000 showed a lower specific surface area compared to NCW, which could be attributed to the introduction of Cu NPs to fill some of the pores of NCW. The specific surface area of $Cu_{1.0}$NPs@NCW-1000 decreased to 582.16 $m^2\ g^{-1}$ with a microporosity of 84.00 % and an average pore size of 2.55

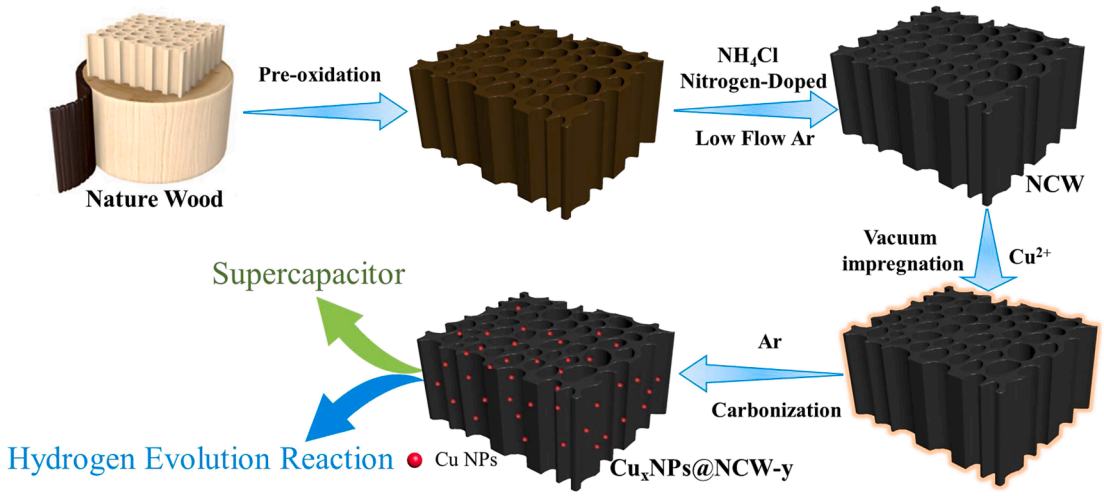

Fig. 1. Schematic diagram of the preparation process of Cu_xNPs@NCW-y.

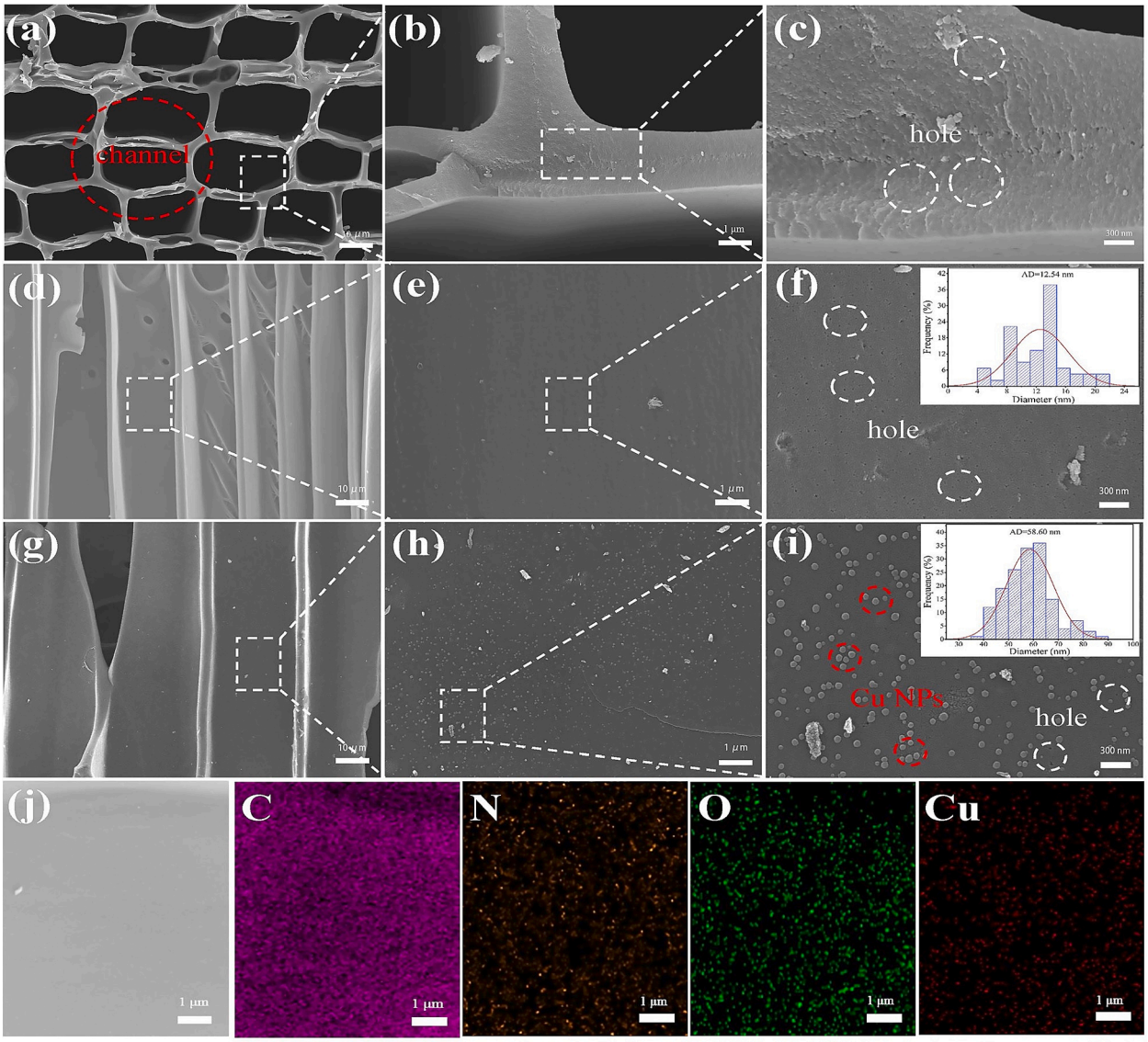

Fig. 2. (a-c) SEM images of nitrogen-doped self-activated carbonized wood electrode (NCW), cross section; (d-f) SEM images of nitrogen-doped self-activated carbonized wood electrode (NCW), vertical section; (g-i) SEM images of $Cu_{1.0}$NPs@NCW-1000 electrode (The inset shows the particle size distribution); (j) Elemental mappings of C, N, O, and Cu for $Cu_{1.0}$NPs@NCW-1000 electrode.

nm (Table S1). Then, the specific surface area of $Cu_{1.0}$NPs@NCW-800 and $Cu_{1.0}$NPs@NCW-600 decreased to 302.19 and 257.90 $m^2\ g^{-1}$, respectively, and the average pore size increased to 2.70 and 3.41 nm with the decrease of annealing temperature during the *in situ* growth of Cu NPs. The microporous area was close to the total specific surface area, which showed a more pronounced microporous nature [17] (Fig. S3a, b, Table S2) and was related to the occurrence of large aggregates of Cu NPs annealed at lower temperatures.

As illustrated in Fig. 3c, the two broad (0 0 2) and (1 0 1) diffraction peaks in SCW and NCW were centered at 23° and 44°, respectively, implying the existence of abundant amorphous carbon in the samples. [30]. Furthermore, the (1 0 1) peak of NCW was weaker, suggesting that nitrogen-doped led to an increase in the spacing of graphitic carbon layers and a decrease in the size of individual graphitic planes [31,32]. Cu_xNPs@NCW-y showed five sharp characteristic peaks at 43.3°, 50.4°, 74.1°, 89.9°, and 95.1°, which was consistent to Cu phase (JCPDS No. 04–0836) (Fig. S4 a, b), which further confirmed the successful preparation of the CuxNPs@NCW-y electrode material. The elemental Cu content of Cu_x NPs@NCW-y obtained at different Cu^{2+} impregnation concentrations was further determined by ICP-OES (Table S3). The results showed that the Cu content in $Cu_{0.5}$NPs@NCW-1000, $Cu_{0.8}$NPs@NCW-1000, $Cu_{1.0}$NPs@NCW-1000 and $Cu_{1.2}$NPs@NCW-1000 was calculated as 9.16 wt%, 16.95 wt%, 19.40 wt%, and 20.23 wt % of the carbonized wood electrodes, respectively, which proved that Cu was decorated on the carbonized wood electrode.

As shown in Fig. 3d, the D band (amorphous carbon) and G band (graphitized carbon) were identified near at 1343 and 1598 cm^{-1}, respectively. The intensity ratio of D-band to G-band (ID/IG) reflected the degree of carbon disorder [28,33]. The calculated ID/IG ratios for SCW, NCW and $Cu_{1.0}$NPs@NCW-1000 were 1.02, 1.08 and 1.06, respectively, and the ID/IG ratios increased substantially with nitrogen-doped, inferring that further etching of NH_3 during nitrogen-doped promoted the growth of defects and disordered portions. Besides, with the uniform growth of Cu NPs, the defect structure of the obtained electrode decreased, which was related to the *in situ* growth of Cu NPs.

Compared to SCW, the N content of NCW and $Cu_{1.0}$NPs@NCW-1000 was significantly higher, and Cu elements were detected in $Cu_{1.0}$NPs@NCW-1000 (Table S4). The XPS survey spectra of $Cu_{1.0}$NPs@NCW-1000 showed the presence of C, O, N and Cu elements (Fig. 3e), demonstrating *in situ* growth of Cu NPs on NCW successfully

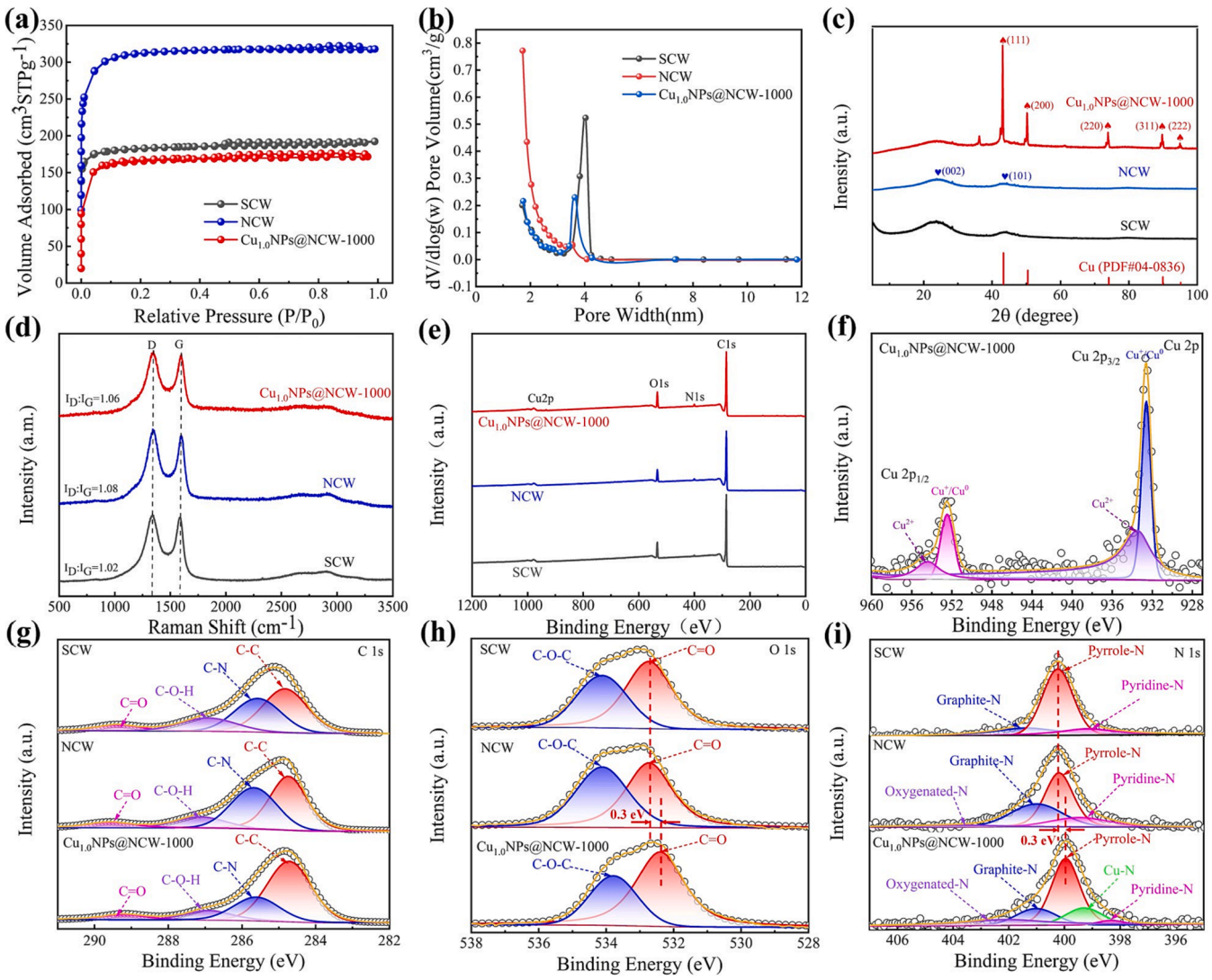

Fig. 3. (a) N_2 adsorption and resolution isotherms, and (b) pore size distribution; (c) XRD patterns; (d) Raman patterns; (e) XPS survey spectrum of SCW, NCW and Cu1.0NPs@NCW-1000; High-resolution XPS spectra of (f) Cu 2p of $Cu_{1.0}$NPs@NCW-1000; XPS spectra of (g) C 1 s, (h) O 1 s, (i) N 1 s of SCW, NCW and $Cu_{1.0}$NPs@NCW-1000.

and further supporting the EDS results. In the Cu 2p spectra of $Cu_{1.0}$NPs@NCW-1000 (Fig. 3f), the peaks observed at 932.6 and 952.5 eV were ascribed to Cu(I)/Cu(0) species, while the weak peaks at 933.7 and 954.4 eV were identified to Cu(II) species. Although the surface analysis revealed a small quantity of oxidized Cu^{2+} present in the air, it was primarily located as Cu monomers [34]. The C 1 s spectra of SCW, NCW, and $Cu_{1.0}$NPs@NCW-1000 showed four peaks located at 284.8, 285.7, 287.2, and 289.2 eV, belonging to C = C (sp2 bond), C-N (sp3 bond), C-O-H, and C = O, respectively [35] (Fig. 3g). For O 1 s, two peaks at 532.7 and 534.1 eV were corresponded to the absorbed C = O and C-O-C bonds, respectively [36] (Fig. 3h). Interestingly, oxygen-containing functional groups, especially carboxyl and carbonyl groups, could enhance the hydrophilicity of the materials, introduce pseudocapacitance to improve capacitance performance, and further improve electrochemical activity [37].

Significantly, the N 1 s spectra (Fig. 3i) showed significant differences between SCW, NCW, and $Cu_{1.0}$NPs@NCW-1000. The N 1 s spectra of SCW were resolved into three peaks with binding energies at 399.1 (pyridine N), 400.3 (pyrrole N), and 401.2 eV (graphite N). Compared to SCW, the N 1 s spectra of NCW added nitrogen oxide at 403.3 eV [36,38,39]. Furthermore, the N 1 s spectrum of $Cu_{1.0}$NPs@NCW-1000 exhibited a peak at 399.2 eV (Cu-N bonds) compared to NCW. This further indicated the successful loading of Cu element, which was favorable for the enhancement of inter-electronic interactions and the improvement of the electrode capacitance and HER performance. Interestingly, the exposed pyrrole-N, pyridine-N, and graphite-N had been reported to play major roles in improving capacitance and catalytic properties because the pyrrole-N was an electron donor that enhances carbon catalytic activity during electron transport, whereas the pyridine-N introduced active sites and the graphite-N promoted electron transport [17,39]. More importantly, compared to SCW and NCW, the N 1 s and O 1 s spectra of $Cu_{1.0}$NPs@NCW-1000 were both slightly shifted to lower binding energies (0.3 eV, Fig. 3h, i), due to the higher electronegativity of N and O compared with that of Cu and the transfer of electrons from the inner core of Cu. This indicated that powerful electronic interactions were established between Cu NPs and NCW, which accelerated the electron transfer inside $Cu_{1.0}$NPs@NCW-1000, and thus promoting the oxidation–reduction reaction and improving the electrochemical performance [40].

3.2. Electrochemical performance for supercapacitors

The capacitive capability of the prepared electrodes was investigated using a three-electrode system in a 2.0 M KOH electrolyte. First, the

cyclic voltammetry (CV) curves of SCW, NCW, and $Cu_{1.0}$NPs@NCW-1000 electrodes exhibited good shapes (Fig. 4a, c, Fig. S5), indicating the remarkable capacitive performance. Compared with SCW and NCW, $Cu_{1.0}$NPs@NCW-1000 obviously possessed a larger closed area, suggesting its highest capacitance. Significantly, during the scan from −1 V to 0 V, two distinct peak currents were shown at −0.45 V and −0.15 V for $Cu_{1.0}$NPs@NCW-1000, which was resulted from the gradual oxidization of Cu^0 to Cu^{2+}. And a large peak current was observed near at −0.51 V in the scanning process from 0 V to −1 V, which was due to the conversion of Cu^{2+} to Cu^0 in the electrode (Fig. 4a), showing that Cu NPs as pseudocapacitive substances had good reversibility in the redox process. In addition, the galvanostatic charge–discharge (GCD) measurements (Fig. 4b, d, Fig S6) showed nearly isosceles triangles in shape, with good capacitance properties. Obviously, the $Cu_{1.0}$NPs@NCW-1000 electrode had the longest discharge time, suggesting the highest specific capacitance, which agreed with the result of the CV analysis. The best capacitive performance might be due to the open channels, uniform growth of Cu NPs, nitrogen-doped, and hierarchical porous structure, which facilitated the penetration of the electrolyte and full exposure of the active sites. Interestingly, the potential slopes of $Cu_{1.0}$NPs@NCW-1000 showed two obvious changes in the GCD curves, which led to the GCD curves deviating from the original ideal smooth curves (Fig. 4b), proving that the Cu/C electrode had pseudocapacitive behaviors [41,42].

Furthermore, as shown in Fig. 4e, $Cu_{1.0}$NPs@NCW-1000 exhibited very high area specific capacitances of 10.39, 9.66, 7.57, 6.13, 5.91, 4.88, and 4.15 F cm^{-2} at 1, 2, 5, 10, 20, and 50 mA cm^{-2}, and 305.57, 284.14, 222.65, 180.29, 173.82, 143.53, and 122.06 F g^{-1} of very high mass specific capacitance, which was superior to the majority of carbon-based electrodes used for supercapacitors (Table S5). Notably, even at high current density of 10 mA cm^{-2}, the $Cu_{1.0}$NPs@NCW-1000 electrode achieved an area specific capacitance of 6.13 F cm^{-2} and a capacitance retention of 59 % with excellent multiplicative performance, which was attributed to the open vertical pipeline facilitating the electrolyte transport. As illustrated in Fig. 4f, the equivalent series resistance Rs (1 Ω) of SCW, NCW and $Cu_{1.0}$NPs@NCW-1000 were all very small, which might be related to the high conductivity produced by annealing at 1000 °C. The increase of pyridine nitrogen species during N doping also led to more defects in the material, but there were too many defect sites in the material, the electrical conductivity decreased to some extent, so that the resistance of SCW appeared to be slightly smaller than that of NCW [43,44]. And the charge transfer resistance Rct (0.12 Ω) of $Cu_{1.0}$NPs@NCW-1000 was the smallest compared to the SCW and NCW. Besides, the Nyquist curve of $Cu_{1.0}$NPs@NCW-1000 showed a straight

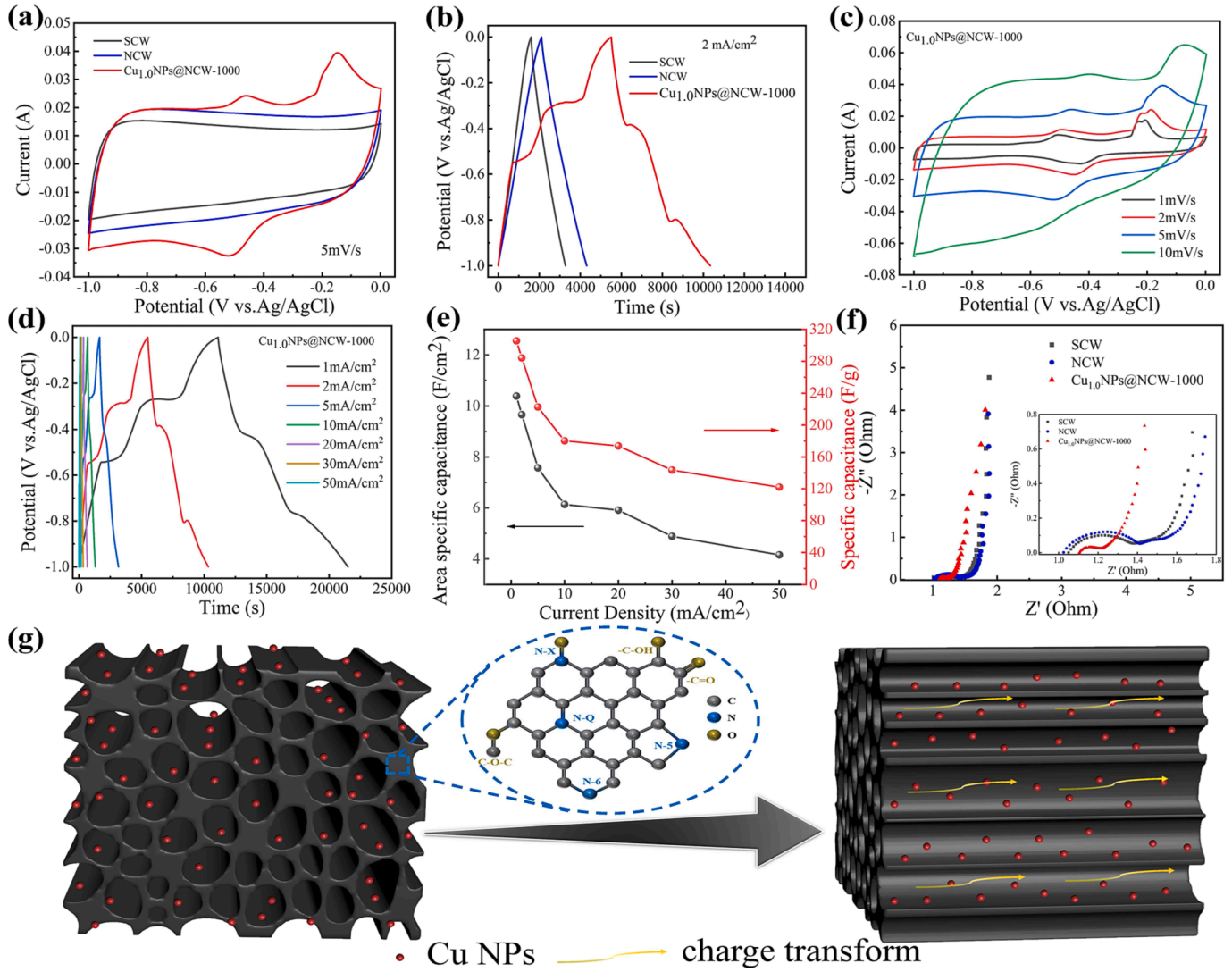

Fig. 4. The performance of SCW, NCW, and $Cu_{1.0}$NPs@NCW-1000 in 2.0 M KOH electrolyte: (a) CV curves at 5 mV s^{-1}; (b) GCD curves at 2 mA cm^{-2}; (c) CV curves of $Cu_{1.0}$NPs@NCW-1000 electrode at 1 to 10 mV s^{-1}; (d) GCD curves of $Cu_{1.0}$NPs@NCW-1000 electrode at 1 to 50 mA cm^{-2}; (e) Specific capacitance of $Cu_{1.0}$NPs@NCW-1000 electrode; (f) EIS spectra; (g) Charge transfer within the $Cu_{1.0}$NPs@NCW-1000 electrode.

and closest-to-vertical slope in the low-frequency region, demonstrating that the electrodes had minimal diffusion resistance and ideal capacitance characteristics [17,45].

Fig. S7 and S8 demonstrated the supercapacitor performance of Cu_xNPs@NCW-y obtained by *in situ* growth of Cu NPs with different Cu^{2+} concentration impregnation and different annealing temperatures. Obviously, $Cu_{1.0}$NPs@NCW-1000 had the largest CV curve area, the longest discharge time, and the smallest charge transfer resistance, thus obtaining the best supercapacitor performance due to the higher specific surface area, the more uniformly grown Cu NPs, and the excellent pore structure. To demonstrate the superior cycling performance of the electrodes, the Cu_xNPs@NCW-y electrodes were tested for 1,000 cycles at 20 mA cm^{-2} (Fig. S7d and S8d). It was demonstrated that the capacitance of $Cu_{1.0}$NPs@NCW-1000 electrode can be maintained at 94.66 % with good reversibility and remained at 90.21 % even after up to 5000 cycles (Fig. S9), was closely related to the uniformly grown Cu NPs as well as the permeability of the pore structure. The SEM images showed that the majority of Cu NPs in the $Cu_{1.0}$NPs@NCW-1000 electrode remained the original particle size after 5000 cycles stability test, and a minority of them produced agglomerations during the redox process of galvanostatic charge–discharge (Fig. S10a), which indicated the $Cu_{1.0}$NPs@NCW-1000 possessed a good stability. In addition, the XRD patterns and XPS spectra of $Cu_{1.0}$ NPs@NCW-1000 before and after 5000 cycles stability test were shown in Fig. S10b and c, respectively. The XRD pattern showed two sharp characteristic peaks at 36.6° and 61.7°, which matched to CuO phase (JCPDS No. 78-0428), attributing to the fact that some of Cu NPs were oxidized during the galvanostatic charge–discharge process to form a small amount of CuO. In the Cu 2p spectrum, the enhancement of the peaks at 933.7 and 954.4 eV was further evidence for the formation of CuO, but the $Cu_{1.0}$NPs@NCW-1000 was still mainly in the form of Cu (0). Fig. 4g showed the schematic diagram of charge transfer during the operation of $Cu_{1.0}$NPs@NCW-1000 electrode. The uniformly grown Cu NPs in the channels of NCW as pseudocapacitive substances increased the active sites, the vertical channels and large number of nanopores of NCW facilitated the penetration and diffusion of the electrolyte, and the inter-electronic interactions between Cu NPs and NCW promoted the charge transfer of supercapacitors. Therefore, the as-prepared electrode possessed the excellent capacitive performance.

Furthermore, a symmetric supercapacitor (SSC) was assembled using the $Cu_{1.0}$NPs@NCW-1000 electrodes, KOH solution (2.0 M) as electrolyte, and filter paper as the diaphragm. In the absence of polarization,

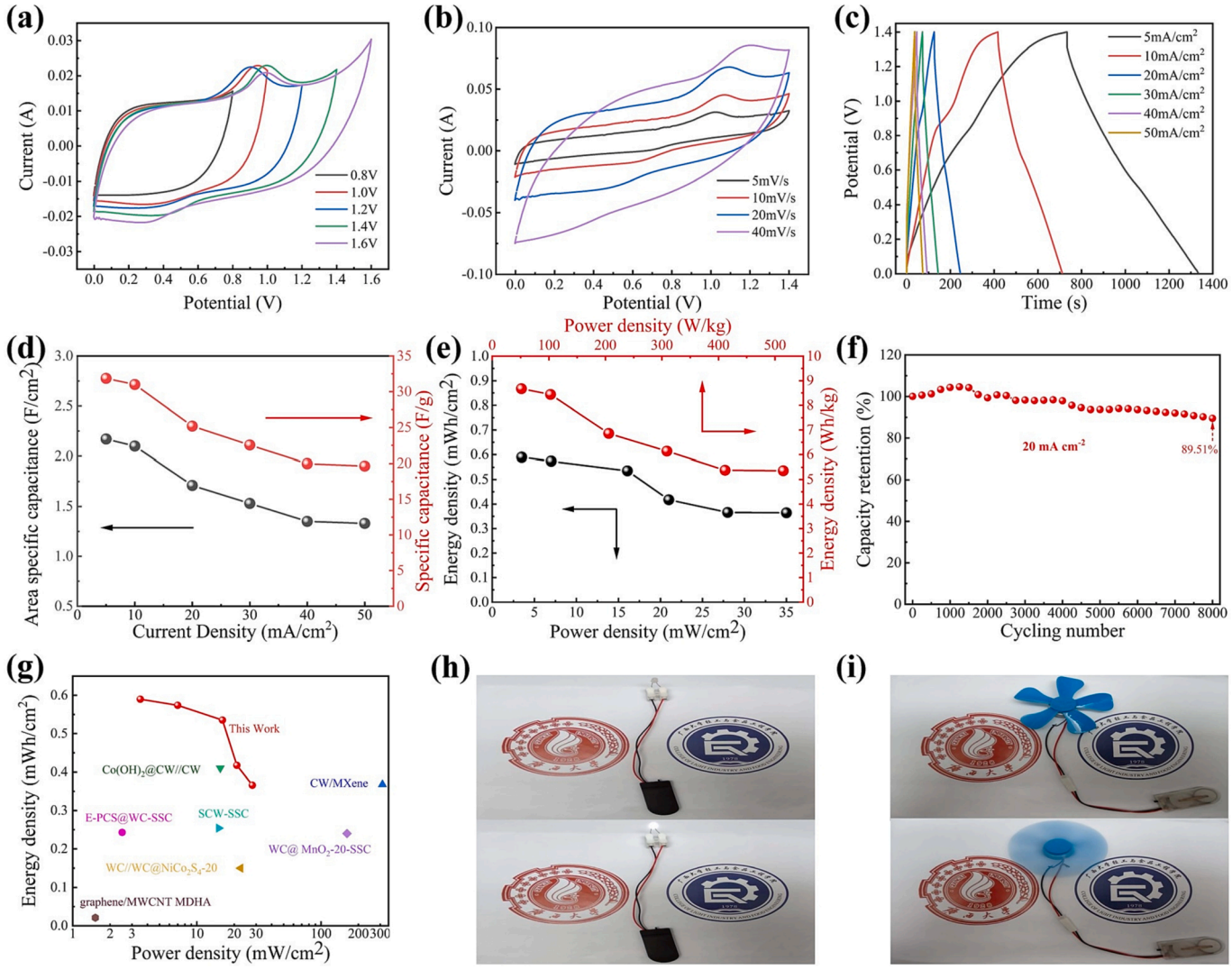

Fig. 5. Capacitive performance of SSC: (a) CV curves of the SSC devices at different potential ranges; (b) CV curves at 1 to 10 mV s^{-1}; (c) GCD curves at 5 to 50 mA cm^{-2}; (d) Multiplicative performance based on different current densities; (e) Power and energy density plot of the SSC; and (f) Cycling stability of the SSC for 8,000 cycles at 20 mA cm^{-2}; (g) The Ragone plot of the SSC for the comparison with the reported supercapacitor devices. (E-PCS@WC-SSC [46], CW/MXene [47], Co$(OH)_2$@CW//CW [48], WC@MnO_2-20-SSC [49], WC//WC@ $NiCo_2S_4$-20 [50], SCW-SSC [25], Graphene/MWCNT MDHA [51]), (h, i) Photo of two SSC devices in series powering an LED or small fan.

the voltage window of the SSC was extended to a maximum of 1.4 V (Fig. 5a). These results suggested that nitrogen-doped played an important role in the stabilization of the interface between the electrode and electrolyte [36]. The CV curves presented a more favorable rectangular shape (Fig. 5b) at 1 to 10 mV s^{-1}, showing outstanding ion transfer diffusion efficiency. Meanwhile, the GCD curves (Fig. 5c) exhibited an ideal isosceles triangle shape with low IR drop at 5 to 50 mA cm^{-2}, showing superior electrochemical performance, good multiplication properties and very low equivalent internal resistance. As shown in Fig. 5d, the SSC showed an outstanding specific capacitance of 2.17 F cm^{-2} (10.87 F cm^{-3} and 31.86 F g^{-1}) at 5 mA cm^{-2}, owing to excellent hierarchical porous structure, the uniformly grown Cu NPs, and high specific surface area of the $Cu_{1.0}$NPs@NCW-1000 electrode. The SSC achieved specific capacitance of 1.33 F cm^{-2} (6.65 F cm^{-3} and 19.66 F g^{-1}) even at 50 mA cm^{-2}. This might be attributed to the fact that the electrode had the vertical channels and a large number of defects induced due to nitrogen doped, which allowed the electrolyte ions to penetrate efficiently even at high charge and discharge rates [17]. More importantly, as shown in Fig. 5e, the SSC showed an energy density of 0.59 mWh cm^{-2} (2.59 mWh cm^{-3} and 8.7 Wh kg^{-1}) at a power density of 3.5 mW cm^{-2} (17.5 mW cm^{-3} and 51.5 W kg^{-1}). These surprising properties exceeded previously reported carbon-based supercapacitors (Fig. 5g). Concurrently, the SSC device exhibited a cycling performance of 89.51 % after 8,000 long-term cycles at 20 mA cm^{-2} (Fig. 5f), conforming the outstanding stability of $Cu_{1.0}$NPs@NCW-1000. Additionally, two SSC devices in series can power LED (1.0 W) and a small fan for 10 min and 40 s, respectively (Fig. 5h, i), which demonstrated its potential for practical applications.

3.3. Electrocatalytic performance for HER

The electrocatalytic properties of the electrodes were examined using a typical three-electrode system under N_2 saturated 1.0 M KOH alkaline conditions. As shown in Fig. 6a, the HER polarization curves of the electrodes were acquired using linear scanning voltammetry (LSV) at 5 mV s^{-1}. The overpotentials of the SCW, NCW, and $Cu_{1.0}$NPs@NCW-1000 samples were 210, 161, and 100.43 mV at 10 mA cm^{-2}, respectively. In addition, the lower overpotential of NCW as compared to SCW might be caused by the fact that the layered porous structure resulting from nitrogen-doped facilitated the escape of gases during the HER process, and nitrogen-doped could change the electronic structure of the material to increase the catalytic activity. The overpotential of

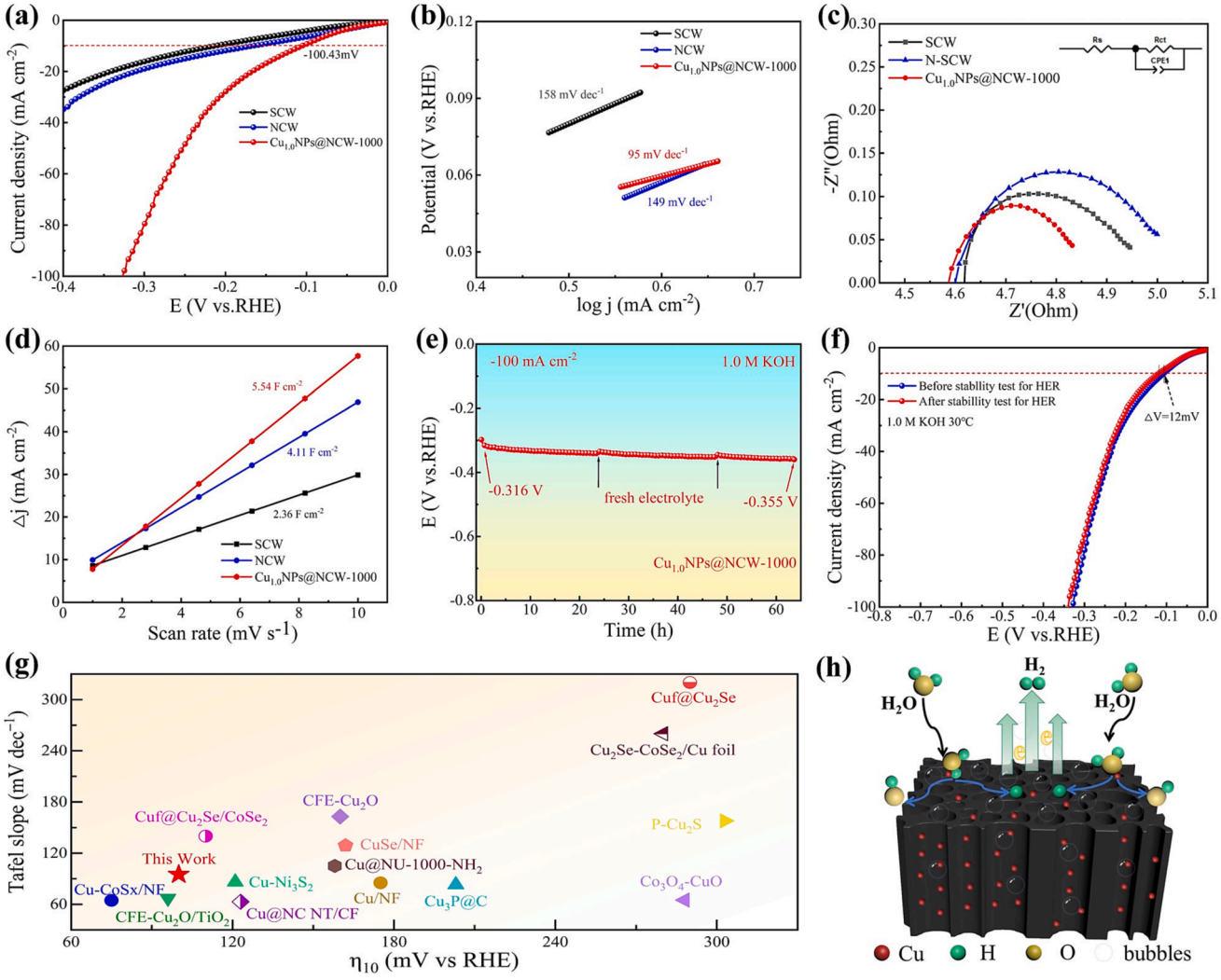

Fig. 6. HER performance of SCW, NCW, and $Cu_{1.0}$NPs@NCW-1000 in 1.0 M KOH electrolyte: (a) polarization curves; (b) Tafel slopes; (c) Nyquist plots; (d) C_{dl} values; (e) CP curves of $Cu_{1.0}$NPs@NCW-1000; (f) LSV curve of $Cu_{1.0}$NPs@N-SCW-1000 before and after CP stability test; and (g) Comparison of the overpotential required to generate 10 mA cm^{-2} current density together with the Tafel slope on $Cu_{1.0}$NPs@N-SCW-1000 and the reported catalysts (Cu-CoSx/NF [22], CFE-Cu_2O/TiO_2 [53], Cuf@Cu_2Se/$CoSe_2$ [54], Cu-Ni_3S_2 [24], Cu@NC NT/CF [55], CFE-Cu_2O [53], CuSe/NF [56], Cu@NU-1000-NH_2 [20], Cu/NF [57], Cu_3P@C [58], Cuf@Cu_2Se [54], Cu_2Se-$CoSe_2$/Cu foil [54], P-Cu_2S [59], Co_3O_4–CuO [60]); (h) Schematic illustration of structure characteristics for the $Cu_{1.0}$NPs@NCW-1000 electrode.

$Cu_{1.0}$NPs@NCW-1000 indicated that the *in situ* uniform growth of Cu NPs significantly enhanced the HER activity of the material, probably due to the synergistic interaction between Cu NPs and nitrogen-doped carbonized wood optimizing the electronic structure of the catalyst, which led to the enhancement of the electrical conductivity and intrinsic activity of the material. The kinetic properties of HER were further examined through fitting the linear part of the LSV curve to acquire the Tafel slope. Furthermore, the Tafel slope of $Cu_{1.0}$NPs@NCW-1000 was only 95 mV dec^{-1}, which was significantly better than NCW (149 mV dec^{-1}) and SCW (158 mV dec^{-1}) (Fig. 6b), indicating $Cu_{1.0}$NPs@NCW-1000 could more easily overcome the kinetic process of HER, which was a Volmer-Heyrovsky reaction with a rate-limiting step of HER process [52]. These good HER properties surpassed most of the previously reported Cu-based catalysts (Fig. 6g and Table S6).

The electrochemical impedance (EIS) was investigated to study the HER kinetics of the electrodes. The Nyquist plots of SCW, NCW, and $Cu_{1.0}$NPs@NCW-1000 were shown in Fig. 6c. The smallest semicircle diameter of $Cu_{1.0}$NPs@NCW-1000 indicated its lowest impedance and demonstrated the interaction between NCW and Cu NPs facilitated the charge transfer so that the interface had an optimal electron transfer rate [61]. Meanwhile, the electrochemical specific surface area (ECSA) was proportional to the capacitance of the double electric layer (C_{dl}), which was an important metric to elucidate the activity of catalysts in HER. The C_{dl} values of SCW, NCW, and $Cu_{1.0}$NPs@NCW-1000 was calculated by the cyclic voltammetry (CV) method in non-Faraday intervals at different scanning speeds (Fig. S11a-c). As shown in Fig. 6d, the C_{dl} value (5.54 F cm^{-2}) of $Cu_{1.0}$NPs@NCW-1000 was higher than that of NCW (4.11 F cm^{-2}) and SCW (2.36 F cm^{-2}), which showed that the *in situ* growth of Cu NPs exposed a larger number of catalytically active sites, thus improved the catalytic activity. In addition, the HER performance of Cu_xNPs@NCW-y obtained by *in situ* growth of Cu NPs with different Cu^{2+} concentration impregnation and different annealing temperatures was demonstrated in Fig. S12–14. Obviously, Cu1.0NPs@NCW-1000 possessed the lowest overpotential, the smallest Tafel slope, the smallest internal resistance to charge transfer, and the largest electrochemical specific surface area.

Furthermore, the electrochemical durability was an important criterion for evaluating the electrocatalysts used for HER. The HER stability of $Cu_{1.0}$NPs@NCW-1000 under 1.0 M KOH was evaluated using the CP method (Fig. 6e). The $Cu_{1.0}$NPs@NCW-1000 was able to work continuously for 65 h at 100 mA cm^{-2} without any significant change in its potential, showing good electrochemical stability. After 65 h of continuous operation, the polarization curves of $Cu_{1.0}$NPs@NCW-1000 almost overlapped with an offset of only 12 mV, showing excellent stability (Fig. 6f). The SEM images showed that after 65 h HER stability test, most of the Cu NPs in $Cu_{1.0}$NPs@NCW-1000 did not show obvious morphological changes (Fig. S15a), which indicated Cu NPs were firmly decorated on the substrate with excellent stability. After 65 h HER stability test, the XRD pattern of $Cu_{1.0}$NPs@NCW-1000 electrode exhibited a weak characteristic peak of CuO (Fig. S15b). In addition, Cu 2p XPS spectra showed that the peaks of Cu^{2+} 2p were relatively enhanced compared to the original $Cu_{1.0}$NPs@NCW-1000 electrodes (Fig. S15c), which could be attributed to the fact that a small portion of the Cu NPs were oxidized to Cu^{2+} during the HER stability tests [57]. These results demonstrated that $Cu_{1.0}$NPs@NCW-1000 exhibited good HER stability in 1.0 M KOH, which showed some value for industrial applications. Cu1.0NPs@NCW-1000 had good HER performance due to its hierarchical porous structure, uniformly distributed nanopores, nitrogen-doped and *in situ* grown Cu NPs, which increased the catalytic active sites, accelerated the gas escape and enhanced the contact between the electrolyte and the active sites. Based on the aforementioned discussion, a schematic diagram of the structural features of $Cu_{1.0}$NPs@NCW-1000 was given in Fig. 6h.

4. Conclusions

In this work, the Cu_xNPs@NCW-y electrodes were successfully prepared by different impregnating concentrations of Cu^{2+} and annealing temperatures. The $Cu_{1.0}$NPs@NCW-1000 electrode obtained with a 1.0 M Cu^{2+} solution impregnation and 1000 °C annealing temperature exhibited the most exceptional electrochemical performance. The $Cu_{1.0}$NPs@NCW-1000 electrode displayed outstanding HER and supercapacitor performance owing to its high specific surface area, uniformly loaded copper nanoparticles, nitrogen doped, excellent layered porous structure, and numerous active sites. The $Cu_{1.0}$NPs@NCW-1000 electrode showed ultra-high specific capacitance of 10.39 F cm^{-2} (305.57 F g^{-1}) at 1 mA cm^{-2}. The assembled symmetric supercapacitor (SSC) showed a high energy density of 0.59 mWh cm^{-2} (8.7 Wh kg^{-1}) at a power density of 3.5 mW cm^{-2} (51.5 W kg^{-1}). The capacitance retention was 89.51 % after 8,000 cycles at 20 mA cm^{-2}, demonstrating superior stability. In addition, $Cu_{1.0}$NPs@NCW-1000 exhibited an excellent HER performance and stability with an overpotential of only 100.43 mV at 10 mA cm^{-2}, the Tafel slope of 95 mV dec^{-1} and a polarization curve shift of only 12 mV after 65 h of continuous operation at 100 mA cm^{-2}. Therefore, this study combined the advantages of non-precious metal nanoparticles with self-supported carbonized wood electrodes to provide good candidates for the energy storage and conversion.

CRediT authorship contribution statement

Hewei Hou: Writing – original draft, Methodology, Investigation, Formal analysis, Data curation. **Huashuang Huo:** Methodology, Investigation, Formal analysis. **Yuanyuan Yu:** Methodology, Investigation, Formal analysis. **Moyan Li:** Formal analysis, Data curation. **Yangyang Chen:** Methodology, Formal analysis. **Changzhou Chen:** Supervision, Methodology, Formal analysis. **Guangfu Qian:** Writing – review & editing, Validation, Supervision, Resources, Methodology, Conceptualization. **Douyong Min:** Writing – review & editing, Validation, Supervision, Resources, Project administration, Conceptualization.

Declaration of competing interest

The authors declare that they have no known competing financial interests or personal relationships that could have appeared to influence the work reported in this paper.

Data availability

Data will be made available on request.

Acknowledgements

This work is supported by the National Natural Science Foundation of China (32371814, 31400514), the China National Key R&D Program (2022YFC2105503), the Young Elite Scientists Sponsorship Program by CAST (2022QNRC001), the Natural Science Foundation of Guangxi (2018JJA130224), and the Opening Project of Guangxi Key Laboratory of Clean Pulp & Papermaking and Pollution Control (2022GXZZKF75).

Appendix A. Supplementary data

Supplementary data to this article can be found online at https://doi.org/10.1016/j.cej.2024.149454.

References

[1] J. Chow, R.J. Kopp, P.R. Portney, Energy resources and global development, Science 302 (2003) 1528–1531.
[2] X. Huang, X. Xu, X. Luan, D. Cheng, CoP nanowires coupled with CoMoP nanosheets as a highly efficient cooperative catalyst for hydrogen evolution reaction, Nano Energy 68 (2020) 104332.

[3] J. Bi, X. Zhai, G. Liu, J.-Q. Chi, X. Wang, S. Chen, Z. Xiao, L. Wang, Low loading of P modified Rh nanoparticles encapsulated in N, P-doped carbon for boosted and pH-universal hydrogen evolution reaction, Int. J. Hydrogen Energy 47 (2022) 3791–3800.

[4] A. Nairan, C. Liang, S.-W. Chiang, Y. Wu, P. Zou, U. Khan, W. Liu, F. Kang, S. Guo, J. Wu, C. Yang, Proton selective adsorption on Pt–Ni nano-thorn array electrodes for superior hydrogen evolution activity, Energ. Environ. Sci. 14 (2021) 1594–1601.

[5] H. Sun, X. Xu, Y. Song, W. Zhou, Z. Shao, Designing high-valence metal sites for electrochemical water splitting, Adv. Funct. Mater. 31 (2021) 2009779.

[6] H. Zhang, Y. Geng, J. Huang, Z. Wang, K. Du, H. Li, Charge and mass transport mechanisms in two-dimensional covalent organic frameworks (2D COFs) for electrochemical energy storage devices, Energ. Environ. Sci. 16 (2023) 889–951.

[7] M. Yi, J. Ma, Y. Ren, H. Wang, L. Xie, Z. Zhu, J. Zhang, Ionic Liquid Meets MOF: A Facile Method to Optimize the Structure of CoSe2-NiSe2 Heterojunctions with N, P, and F Triple-Doped Carbon Using Ionic Liquid for Efficient Hydrogen Evolution and Flexible Supercapacitors, Advanced, Science 10 (2023) 2206029.

[8] Y. Zhu, J. Ma, P. Das, S. Wang, Z.-S. Wu, High-voltage MXene-based supercapacitors: present status and future perspectives, Small Methods. 7 (2023) 2201609.

[9] Q. Zhu, D. Zhao, M. Cheng, J. Zhou, K.A. Owusu, L. Mai, Y. Yu, A New View of Supercapacitors: Integrated Supercapacitors, Adv. Energy Mater. 9 (2019) 1901081.

[10] N. Choudhary, C. Li, J. Moore, N. Nagaiah, L. Zhai, Y. Jung, J. Thomas, Supercapacitors: Asymmetric Supercapacitor Electrodes and Devices, Adv. Mater. 29 (2017) 1605336.

[11] D. Vikraman, S. Hussain, I. Rabani, A. Feroze, M. Ali, Y.-S. Seo, S.-H. Chun, J. Jung, H.-S. Kim, Engineering $MoTe_2$ and Janus SeMoTe nanosheet structures: First-principles roadmap and practical uses in hydrogen evolution reactions and symmetric supercapacitors, Nano Energy 87 (2021) 106161.

[12] D. Kobina Sam, E. Kobina Sam, X. Lv, Application of biomass-derived nitrogen-doped carbon aerogels in electrocatalysis and supercapacitors, ChemElectroChem 7 (2020) 3695–3712.

[13] Y. Feng, J. Jiang, Y. Xu, S. Wang, W. An, Q. Chai, U.H. Prova, C. Wang, G. Huang, Biomass derived diverse carbon nanostructure for electrocatalysis, energy conversion and storage, Carbon 211 (2023) 118105.

[14] X. Han, H. Jiang, Y. Zhou, W. Hong, Y. Zhou, P. Gao, R. Ding, E. Liu, A high performance nitrogen-doped porous activated carbon for supercapacitor derived from pueraria, J. Alloy. Compd. 744 (2018) 544–551.

[15] S. Yoo, S.Y. Jeong, J.-W. Lee, J.H. Park, D.-W. Kim, H.J. Jeong, J.T. Han, G.-W. Lee, S.Y. Jeong, Heavily nitrogen doped chemically exfoliated graphene by flash heating, Carbon 144 (2019) 675–683.

[16] D. Guo, J. Qian, R. Xin, Z. Zhang, W. Jiang, G. Hu, M. Fan, Facile synthesis of nitrogen-enriched nanoporous carbon materials for high performance supercapacitors, J. Colloid Interface Sci. 538 (2019) 199–208.

[17] F. Liu, Y. Gao, C. Zhang, H. Huang, C. Yan, X. Chu, Z. Xu, Z. Wang, H. Zhang, X. Xiao, W. Yang, Highly microporous carbon with nitrogen-doping derived from natural biowaste for high-performance flexible solid-state supercapacitor, J. Colloid Interface Sci. 548 (2019) 322–332.

[18] M. Hu, Z. Wang, M. Li, K. Pan, L. Li, Nano-pom-pom multiphasic MoS_2 grown on carbonized wood as electrode for efficient hydrogen evolution in acidic and alkaline media, Int. J. Hydrogen Energy 46 (2021) 28087–28097.

[19] P.M. Pandian, A. Pandurangan, Copper nanoparticles anchored onto boron-doped graphene nanosheets for use as a high performance asymmetric solid-state supercapacitor, RSC Adv. 9 (2019) 3443–3461.

[20] R.K. Aparna, A. Karmakar, R.T. Arsha, S. Kundu, S. Mandal, Copper nanoparticle-embellished Zr-based metal–organic framework for electrocatalytic hydrogen evolution reaction, Chem. Commun. 59 (2023) 10444–10447.

[21] S.R. Stoyanov, A.V. Titov, P. Král, Transition metal and nitrogen doped carbon nanostructures, Coord. Chem. Rev. 253 (2009) 2852–2871.

[22] H. He, L. Zeng, X. Peng, Z. Liu, D. Wang, B. Yang, Z. Li, L. Lei, S. Wang, Y. Hou, Porous cobalt sulfide nanosheets arrays with low valence copper incorporated for boosting alkaline hydrogen evolution via lattice engineering, Chem. Eng. J. 451 (2023) 138628.

[23] J. Zhang, J. Lian, Q. Jiang, G. Wang, Boosting the OER/ORR/HER activity of Ru-doped Ni/Co oxides heterostructure, Chem. Eng. J. 439 (2022) 135634.

[24] L. Zhang, X. Gao, Y. Zhu, A. Liu, H. Dong, D. Wu, Z. Han, W. Wang, Y. Fang, J. Zhang, Z. Kou, B. Qian, T.-T. Wang, Electrocatalytically inactive copper improves the water adsorption/dissociation on Ni_3S_2 for accelerated alkaline and neutral hydrogen evolution, Nanoscale 13 (2021) 2456–2464.

[25] Y. Chen, Y. Yu, X. Zhang, C. Guo, C. Chen, S. Wang, D. Min, High performance supercapacitors assembled with hierarchical porous carbonized wood electrode prepared through self-activation, Ind. Crop. Prod. 181 (2022) 114802.

[26] C. Mao, Z. Shi, J. Peng, L. Ou, Y. Chen, J. Huang, Hierarchically Porous Carbonized Wood Decorated with MoNi4-Embedded MoO2 Nanosheets: An Efficient Electrocatalyst for Water Splitting, Adv. Funct. Mater. 2308337 (2023).

[27] M. Yao, B. Wang, B. Sun, L. Luo, Y. Chen, J. Wang, N. Wang, S. Komarneni, X. Niu, W. Hu, Rational design of self-supported Cu@WC core-shell mesoporous nanowires for pH-universal hydrogen evolution reaction, Appl. Catal. B 280 (2021) 119451.

[28] A.R. Selvaraj, A. Muthusamy, C. Inho, H.-J. Kim, K. Senthil, K. Prabakar, Ultrahigh surface area biomass derived 3D hierarchical porous carbon nanosheet electrodes for high energy density supercapacitors, Carbon 174 (2021) 463–474.

[29] Z. Shi, C. Mao, L. Zhong, J. Peng, M. Liu, H. Li, J. Huang, Mo-doped Ni_3S_4 nanosheets grown on carbonized wood as highly efficient and durable electrocatalysts for water splitting, Appl. Catal. B 339 (2023) 123123.

[30] M. Sevilla, G.A. Ferrero, A.B. Fuertes, Beyond KOH activation for the synthesis of superactivated carbons from hydrochar, Carbon 114 (2017) 50–58.

[31] S. Cheng, B. Chen, L. Qin, Y. Zhang, G. Gao, M. He, Cross-linked poly(ionic liquid) as precursors for nitrogen-doped porous carbons, RSC Adv. 9 (2019) 8137–8145.

[32] X. Deng, B. Zhao, L. Zhu, Z. Shao, Molten salt synthesis of nitrogen-doped carbon with hierarchical pore structures for use as high-performance electrodes in supercapacitors, Carbon 93 (2015) 48–58.

[33] D. Han, Y. Jiao, W. Han, G. Wu, T. Li, D. Yang, A. Dong, A molecular-based approach for the direct synthesis of highly-ordered, homogeneously-doped mesoporous carbon frameworks, Carbon 140 (2018) 265–275.

[34] D. Cheng, X. Bai, J. Pan, J. Wu, J. Ran, G. Cai, X. Wang, In situ hydrothermal growth of Cu NPs on knitted fabrics through polydopamine templates for heating and sensing, Chem. Eng. J. 382 (2020) 123036.

[35] Z. Tang, Z. Pei, Z. Wang, H. Li, J. Zeng, Z. Ruan, Y. Huang, M. Zhu, Q. Xue, J. Yu, C. Zhi, Highly anisotropic, multichannel wood carbon with optimized heteroatom doping for supercapacitor and oxygen reduction reaction, Carbon 130 (2018) 532–543.

[36] Z. Li, X. Wang, Z. Wang, L. Wang, Y. Guo, C. Zhou, X. Li, K. Du, Y. Luo, Nickel-cobalt layered double hydroxide nanosheets anchored to the inner wall of wood carbon tracheids by nitrogen-doped atoms for high-performance supercapacitors, J Colloid Interface Sci. 608 (2022) 70–78.

[37] X. Li, Y. Jiang, P. Wang, Y. Mo, W. Lai, Z. Li, R. Yu, Y. Du, X. Zhang, Y. Chen, Effect of the oxygen functional groups of activated carbon on its electrochemical performance for supercapacitors, Carbon 171 (2021) 980–981.

[38] K. Zou, Y. Deng, J. Chen, Y. Qian, Y. Yang, Y. Li, G. Chen, Hierarchically porous nitrogen-doped carbon derived from the activation of agriculture waste by potassium hydroxide and urea for high-performance supercapacitors, J. Power Sources 378 (2018) 579–588.

[39] W. Yang, W. Yang, A. Song, L. Gao, L. Su, G. Shao, Supercapacitance of nitrogen-sulfur-oxygen co-doped 3D hierarchical porous carbon in aqueous and organic electrolyte, J. Power Sources 359 (2017) 556–567.

[40] R. Hu, L. Jiao, H. Liang, Z. Feng, B. Gao, X.F. Wang, X.Z. Song, L.Z. Liu, Z. Tan, Engineering Interfacial Built-in Electric Field in Polymetallic Phosphide Heterostructures for Superior Supercapacitors and Electrocatalytic Hydrogen Evolution, Small 19 (2023) 2304132.

[41] J. Gao, J. Hou, L. Kong, Pure Cu particle obtained by ammonia reduction reaction: A new class of electrodes for hybrid supercapacitors, J. Storage Mater. 39 (2021).

[42] S. Teng, G. Siegel, M. Prestgard, W. Wang, A. Tiwari, Synthesis and characterization of copper-infiltrated carbonized wood monoliths for supercapacitor electrodes, Electrochim. Acta 161 (2015) 343–350.

[43] E. Suslova, E. Arkhipova, A. Kalashnik, A. Ivanov, S. Savilov, H. Xia, V. Lunin, Effect of the functionalization of nitrogen-doped carbon nanotubes on electrical conductivity, Russ. J. Phys. Chem. A 1952–1956 (2019).

[44] H. Chen, F. Sun, J. Wang, W. Li, W. Qiao, L. Ling, D. Long, Nitrogen doping effects on the physical and chemical properties of mesoporous carbons, J. Phys. Chem. C 117 (2013) 8318–8328.

[45] F. Wang, J.Y. Cheong, Q. He, G. Duan, S. He, L. Zhang, Y. Zhao, I.-D. Kim, S. Jiang, Phosphorus-doped thick carbon electrode for high-energy density and long-life supercapacitors, Chem. Eng. J. 414 (2021) 128767.

[46] J. Ouyang, X. Wang, L. Wang, W. Xiong, M. Li, Z. Hua, L. Zhao, C. Zhou, X. Liu, H. Chen, Y. Luo, Construction of a porous carbon skeleton in wood tracheids to enhance charge storage for high-performance supercapacitors, Carbon 196 (2022) 532–539.

[47] W. Yao, D. Zheng, Z. Li, Y. Wang, H. Tan, Y. Zhang, MXene@ carbonized wood monolithic electrode with hierarchical porous framework for high-performance supercapacitors, Appl. Surf. Sci. 638 (2023) 158130.

[48] Y. Wang, X. Lin, T. Liu, H. Chen, S. Chen, Z. Jiang, J. Liu, J. Huang, M. Liu, Wood-derived hierarchically porous electrodes for high-performance all-solid-state supercapacitors, Adv. Funct. Mater. 28 (2018) 1806207.

[49] L. Chen, F. Wang, Z. Tian, H. Guo, C. Cai, Q. Wu, H. Du, K. Liu, Z. Hao, S. He, G. Duan, S. Jiang, Wood-derived high-mass-loading MnO2 composite carbon electrode enabling high energy density and high-rate supercapacitor, Small 18 (2022) 2201307.

[50] F. Wang, X. Liu, G. Duan, H. Yang, J.Y. Cheong, J. Lee, J. Ahn, Q. Zhang, S. He, J. Han, Y. Zhao, I.D. Kim, S. Jiang, Wood-derived, conductivity and hierarchical pore integrated thick electrode enabling high areal/volumetric energy density for hybrid capacitors, Small 17 (2021) 2102532.

[51] X. Tang, H. Zhou, Z. Cai, D. Cheng, P. He, P. Xie, D. Zhang, T. Fan, Generalized 3D printing of graphene-based mixed-dimensional hybrid aerogels, ACS Nano 12 (2018) 3502–3511.

[52] Y. Li, H. Wang, L. Xie, Y. Liang, G. Hong, H. Dai, MoS_2 nanoparticles grown on graphene: an advanced catalyst for the hydrogen evolution reaction, J. Am. Chem. Soc. 133 (2011) 7296–7299.

[53] B. Long, H. Yang, M. Li, M.-S. Balogun, W. Mai, G. Ouyang, Y. Tong, P. Tsiakaras, S. Song, Interface charges redistribution enhanced monolithic etched copper foam-based Cu_2O layer/TiO_2 nanodots heterojunction with high hydrogen evolution electrocatalytic activity, Appl Catal B 243 (2019) 365–372.

[54] M. Das, G. Kumar, R.S. Dey, Electrochemical growth and formation mechanism of Cu_2Se/$CoSe_2$-based bifunctional electrocatalyst: a strategy for the development of efficient material toward water electrolysis, ACS Applied Energy Materials. 5 (2022) 3915–3925.

[55] Y. Zhang, Y. Ma, Y.-Y. Chen, L. Zhao, L.-B. Huang, H. Luo, W.-J. Jiang, X. Zhang, S. Niu, D. Gao, J. Bi, G. Fan, J.-S. Hu, Encased copper boosts the electrocatalytic activity of N-Doped carbon nanotubes for hydrogen evolution, ACS Appl. Mater. Interfaces 9 (2017) 36857–36864.

[56] B. Chakraborty, R. Beltrán-Suito, V. Hlukhyy, J. Schmidt, P.W. Menezes, M. Driess, Crystalline copper selenide as a reliable non-noble Electro(pre)catalyst for overall water splitting, ChemSusChem 13 (2020) 3222–3229.
[57] M. Yang, Y. Wang, Y. Gu, Z. Xue, J. Shi, W. An, Y. Rui, Electro-deposited copper nanoclusters on leaf-shaped cobalt phosphide for boosting hydrogen evolution reaction, J. Alloy. Compd. 902 (2022) 163771.
[58] M. Pi, T. Yang, S. Wang, S. Chen, One-pot synthesis of in situ carbon-decorated Cu3P particles with enhanced electrocatalytic hydrogen evolution performance, J. Mater. Res. 33 (2017) 546–555.
[59] D. Yang, L. Cao, J. Huang, Q. Liu, G. Li, D. He, J. Wang, L. Feng, Vanadium-doped hierarchical Cu_2S nanowall arrays assembled by nanowires on copper foam as an efficient electrocatalyst for hydrogen evolution reaction, Scr. Mater. 196 (2021) 113756.
[60] A. Tahira, Z.H. Ibupoto, M. Willander, O. Nur, Advanced Co_3O_4–CuO nano-composite based electrocatalyst for efficient hydrogen evolution reaction in alkaline media, Int. J. Hydrogen Energy 44 (2019) 26148–26157.
[61] J. Bang, I.K. Moon, Y.-K. Kim, J. Oh, Heterostructured Mo2N–Mo2C Nanoparticles Coupled with N-Doped Carbonized Wood to Accelerate the Hydrogen Evolution Reaction, Small Structures. 4 (2023) 2200283.